Toroidal high-spin isomers in the nucleus ^{304}120

A. Staszczak, Cheuk-Yin Wong, and A. Kosior

Phys. Rev. C **95**, 054315 — Published 22 May 2017

DOI: 10.1103/PhysRevC.95.054315

Toroidal high-spin isomers in the nucleus $^{304}120$

A. Staszczak,[1] Cheuk-Yin Wong,[2] and A. Kosior[1]
[1] *Institute of Physics, Maria Curie-Skłodowska University,*
pl. M. Curie-Skłodowskiej 1, 20-031 Lublin, Poland
[2] *Physics Division, Oak Ridge National Laboratory, Oak Ridge, TN 37830, USA*

(Dated: April 30, 2017)

Background: Strongly deformed oblate superheavy nuclei form an intriguing region where the toroidal nuclear structures may bifurcate from the oblate spheroidal shape. The bifurcation may be facilitated when the nucleus is endowed with a large angular moment about the symmetry axis with $I = I_z$. The toroidal high-K isomeric states at their local energy minima can be theoretically predicted using the cranked self-consistent Skyrme-Hartree-Fock method.

Purpose: We use the cranked Skyrme-Hartree-Fock method to predict the properties of the toroidal high-spin isomers in the superheavy nucleus $^{304}120_{184}$.

Method: Our method consists of three steps: first, we use the deformation-constrained Skyrme-Hartree-Fock-Bogoliubov approach to search for the nuclear density distributions with toroidal shapes. Next, using these toroidal distributions as starting configurations we apply an additional cranking constraint of a large angular momentum $I = I_z$ about the symmetry z-axis and search for the energy minima of the system as a function of the deformation. In the last step, if a local energy minimum with $I = I_z$ is found, we perform at this point the cranked symmetry- and deformation-unconstrained Skyrme-Hartree-Fock calculations to locate a stable toroidal high-spin isomeric state in free convergence.

Results: We have theoretically located two toroidal high-spin isomeric states of $^{304}120_{184}$ with an angular momentum $I{=}I_z{=}81\hbar$ (proton 2p-2h, neutron 4p-4h excitation) and $I{=}I_z{=}208\hbar$ (proton 5p-5h, neutron 8p-8h) at the quadrupole moment deformations $Q_{20} = -297.7$ b and $Q_{20} = -300.8$ b with energies 79.2 MeV and 101.6 MeV above the spherical ground state, respectively. The nuclear density distributions of the toroidal high-spin isomers $^{304}120_{184}(I_z{=}81\hbar$ and $208\hbar)$ have the maximum density close to the nuclear matter density, 0.16 fm^{-3}, and a torus major to minor radius aspect ratio $R/d = 3.25$.

Conclusions: We demonstrate that aligned angular momenta of $I_z{=}81\hbar$ and $208\hbar$ arising from multi-particle-multi-hole excitations in the toroidal system of $^{304}120_{184}$ can lead to high-spin isomeric states, even though the toroidal shape of $^{304}120_{184}$ without spin is unstable. Toroidal energy minima without spin may be possible for superheavy nuclei with higher atomic numbers, $Z \gtrsim 122$, as reported previously [7].

PACS numbers: 21.60.Jz, 27.90.+b

I. INTRODUCTION

The landscape of the total energy surface of a nucleus in the deformation degrees of freedom is central to our understanding of the equilibrium shapes and the evolutionary paths in nuclear dynamics. In Fig. 1 one can see the total energy surface for the superheavy nucleus $^{304}120_{184}$ as a function of the quadrupole and octupole degrees of freedom calculated in the constrained Hartree-Fock-Bogoliubov (HFB) approach with the Skyrme energy density functional. In addition to the spherical ground state minimum, the landscape contains the symmetric-elongated-fission (sEF) and asymmetric-elongated-fission (aEF) paths leading to fission. These features have important experimental implications in the multimodal fission decay properties of heavy and superheavy nuclei (*cf.* Refs. [1–3]).

The potential energy surface in Fig. 1 pertains to reflection-symmetric and reflection-asymmetric prolate shapes. How does the energy surface look like in the oblate deformation region? What kinds of the nuclear (equilibrium) shapes may there be in this oblate deformation region?

To gain the proper perspective, it is informative to discuss some general features of our results in the prolate and oblate regions and then examine in details in this paper how oblate region results are obtained. The total HFB energy of $^{304}120_{184}$ as a function of the quadrupole moment Q_{20} is shown in Fig. 2. On the prolate deformation side, the pre-scission density configurations for the sEF and aEF paths are shown at the ends of both paths (at $Q_{20} \approx 360$ b for sEF and $Q_{20} \approx 650$ b for aEF). The effects of triaxiality on the change of the inner and outer axial-symmetric barriers are shown in the insert of Fig. 2. On the oblate deformation side with a negative Q_{20}, one starts from the energy minimum for a spherical ground state to go to the higher energies for oblate spheroids. As the oblate Q_{20} magnitude increases, the oblate spheroidal density changes into a biconcave disc with flattened center density. At $Q_{20} \approx -200$ b, the biconcave disc energy surface reaches an energy about 72 MeV above the spherical ground state. Upon a further increase in the oblate deformation a sudden shape transition from a biconcave disc to a torus takes place with a reduction of the total energy of the nucleus by 10.8 MeV.

The geometry of the toroidal nuclear densities can be characterized by the aspect ratio R/d, where R is the major radius, the distance from the center of the torus hole to the center of the torus tube, and d is the minor radius, the radius of the tube. As is shown in Fig. 2 for $Q_{20} \leq$ -158 b, the aspect ratio R/d of the toroidal solution of the Skyrme-HFB model increases as the oblate Q_{20} magnitude increases.

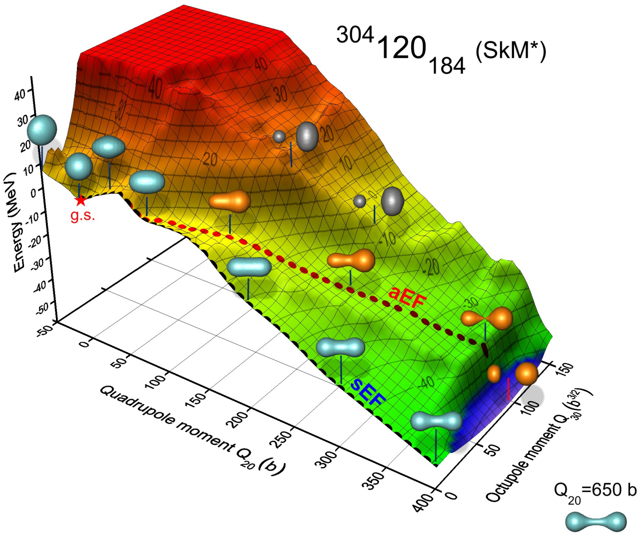

FIG. 1. (Color online) Total HFB energy surface of $^{304}120_{184}$ as a function of the quadrupole Q_{20} and octupole Q_{30} moments. The HFB energy is normalized to the ground state energy. The dashed lines show the symmetric (sEF) and asymmetric elongated fission (aEF) paths along different valleys.

With regard to the emergence of toroidal nuclear matter densities, Wheeler suggested long ago that under appropriate conditions the nuclear fluid may assume a toroidal shape [4]. Conditions that are favorable for the formation of nuclei with a toroidal shape are the cases of excess charge, excess angular momentum, and nuclear shell effects [5, 6]. In the semi-classical liquid-drop model, nuclei with a toroidal shape begin to develop as the fissility parameter x exceeds 0.964. However, the toroidal nucleus is plagued with various instabilities [5], and the search for toroidal nuclei continues [7]. When a toroidal nuclear system is endowed with an angular momentum along the symmetry axis, I=I_z, the variation of the rotational energy of the spinning nucleus can counterbalance the variation of the toroidal bulk energy to lead to toroidal isomeric states at their local energy minima, when the angular momentum I=I_z is beyond a threshold value [6]. A rotating liquid-drop toroidal nucleus can also be stable against sausage instabilities (know also as Plateau-Rayleigh instabilities, in which the torus breaks into smaller fragments [8, 9]), when the same mass flow is maintained across the toroidal meridian to lead to high-spin isomers within an angular momentum window [6].

The rotating liquid-drop model is useful as an intuitive, qualitative guide to point out the essential balance of forces leading to possible toroidal figures of equilibrium. The quantitative assessment of toroidal high-spin isomer (THSI) relies on microscopic descriptions that include both the bulk properties of the nucleus and the single-particle shell effects in self-consistent mean-field theories, such as the Skyrme-Hartree-Fock (Skyrme-HF) approach. Self-consistent mean-field theories are needed because non-collective rotation with an angular momentum about the symmetry axis is permissible quantum mechanically for an axially symmetric toroid only by making single-particle particle-hole excitations to align the angular momenta of the constituents along the symmetry axis [10–15]. As a consequence, only a certain discrete, quantized set of total angular momentum I=I_z states is allowed. We shall adopt the simplified notation that all spins and angular momenta are implicitly in units of $\hbar$ except otherwise explicitly indicated to resolve ambiguities.

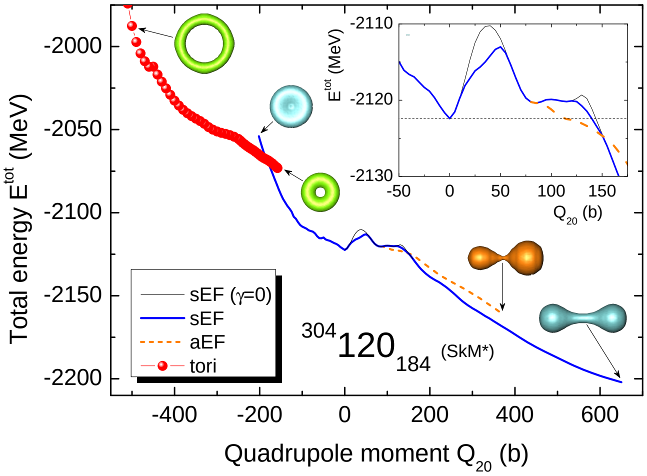

FIG. 2. (Color online) Total HFB energy curve of $^{304}120_{184}$ as a function of the quadrupole moment. The thick solid (blue color) and gray dashed (orange) lines show the symmetric (sEF) and asymmetric (aEF) elongated fission pathways along different valleys, respectively. The effect of triaxiality on the inner and outer barrier is shown in the inset, where the axially symmetric sEF ($\gamma = 0°$) fission pathway is marked by solid thin (black) line. The nuclear matter density distributions with toroidal shapes appear at the region of large oblate deformation $Q_{20} \leqslant -158$ b dark gray (red) solid circles.

It was recently found that the THSI with I=60 may be in the local energy minimum in the excited states of ^{40}Ca by using a cranked Skyrme-HF method starting from the initial ring configuration of 10 alpha particles [16, 17]. Using a cranked Skyrme-HF approach, it was found that toroidal high-spin isomeric states have actually a rather general occurrence for an extended region of even-even light nuclei with $28 \leqslant A \leqslant 52$ [18]. With different rings of alpha particles as initial states, it was also subsequently confirmed that there are THSIs solutions in the extended region of $36 \leqslant A \leqslant 52$ [19]. The particle-hole nature of the light high-spin toroidal isomers has been examined in Ref. [20], the toroidal high-spin isomers with $N \neq Z$ have been located [21], and the THSIs in ^{56}Ni have been described in Ref. [22]. For the nucleus ^{24}Mg, a toroidal diabetic excited state without spin has also been found [23].

In addition to the high-spin toroidal isomers in the light mass region, the superheavy nuclei with large atomic numbers provides another favorable region for toroidal nuclei formation, because the large Coulomb repulsion tends to push the nuclear matter outward to make it energetically advantageous to assume a toroidal shape. A previous work in the superheavy region in the self-consistent constraint Skyrme Hartree-Fock+BCS (Skyrme-HF+BCS) framework indicates that toroidal energy minima are present at various energies as the atomic number increases beyond $Z \gtrsim 122$ [7]. For example, the superheavy nuclei $^{316}122_{194}$, $^{340}130_{210}$, and $^{352}134_{218}$ have toroidal local potential energy minima lying at about 50, 25, and 12 MeV above their corresponding deformed oblate ground state energy minimum, respectively. The superheavy nucleus $^{364}138_{226}$ has a toroidal local potential energy minimum that lies even below the oblate spheroidal energy minimum.

Our purpose in the present manuscript is to explore the closed-shell superheavy nucleus $^{304}120_{184}$ which is localized close to the center of the "island of stability"(*cf.* Refs. [3, 24]). Toroidal system of $^{304}120_{184}$ without a spin may not be stable [25]. It is of interest to find out whether the superheavy nucleus $^{304}120_{184}$ with a toroidal density may become stabilized by the addition of a large nuclear spin.

This manuscript is organized as follows. In Secs. II A-C, we describe the theoretical model. In Sec. III A, we examine properties of the toroidal system of $^{304}120_{184}$ without spin and study the single-particle states in the constrained Skyrme-HFB calculations as a function of the quadrupole moment. In Sec. III B, we present results of the cranked Skyrme-HF calculations for $^{304}120_{184}$ with a toroidal density and a spin. The properties of $^{304}120_{184}$ toroidal high-spin isomers are presented in Sec. III C. Finally, we summarize our studies in Sec. VI.

II. DESCRIPTION OF THE MODEL

A. The Skyrme energy density functional

In the local density approximation the Skyrme energy density functional (EDF), up to second-order in derivatives of the density (*i.e.*, the most general quadratic EDF), can be expressed in terms of seven proton and neutron local densities: the particle (scalar) density $\rho_q(\boldsymbol{r})$, kinetic energy (scalar) density $\tau_q(\boldsymbol{r})$, spin-current (pseudotensor) density $\mathbb{J}_q(\boldsymbol{r})$, current (vector) density $\boldsymbol{j}_q(\boldsymbol{r})$, spin (pseudovector) density $\boldsymbol{s}_q(\boldsymbol{r})$, spin-kinetic (pseudovector) density $\boldsymbol{T}_q(\boldsymbol{r})$, and tensor-kinetic (pseudovector) density $\boldsymbol{F}_q(\boldsymbol{r})$, where $q = \{p, n\}$, see Refs. [26–29].

The above local densities are all real, and $\rho_q(\boldsymbol{r})$, $\tau_q(\boldsymbol{r})$, and $\mathbb{J}_q(\boldsymbol{r})$ are time-even, whereas $\boldsymbol{j}_q(\boldsymbol{r})$, $\boldsymbol{s}_q(\boldsymbol{r})$, $\boldsymbol{T}_q(\boldsymbol{r})$, and $\boldsymbol{F}_q(\boldsymbol{r})$ are time-odd. The spin-current pseudotensor density $\mathbb{J}_q(\boldsymbol{r})$ can be decomposed into trace, antisymmetric and symmetric parts, giving the pseudoscalar $\mathcal{J}_q(\boldsymbol{r})$, vector $\boldsymbol{J}_q(\boldsymbol{r})$, and (traceless) pseudotensor $\mathfrak{J}_q(\boldsymbol{r})$ densities, respectively.

The time reversal and spatial symmetries impose restrictions on the local densities [30, 31]. In spherical nuclei (the rotational and mirror symmetry, O(3)) the pseudoscalar $\mathcal{J}_q(\boldsymbol{r})$, all the pseudovector ($\boldsymbol{s}_q(\boldsymbol{r})$, $\boldsymbol{T}_q(\boldsymbol{r})$, $\boldsymbol{F}_q(\boldsymbol{r})$) and the pseudotensor $\mathfrak{J}_q(\boldsymbol{r})$ local densities vanish. In the case of axial- and reflection-symmetry only the pseudoscalar component $\mathcal{J}_q(\boldsymbol{r})$ vanishes. For the description of static properties in even-even nuclei, all the time-odd densities must vanish to preserve the time-reversal invariance of the density matrix in the particle-hole channel.

The standard proton-neutron separable Skyrme EDF can be divided into two parts, built of the seven isoscalar (t=0) and seven isovector T_z=0 component (t=1) single-particle densities [30]

$$E_{Sk} = \sum_{t=0,1} \int \mathrm{d}^3\boldsymbol{r} \left(\mathcal{H}_t^{even}(\boldsymbol{r}) + \mathcal{H}_t^{odd}(\boldsymbol{r}) \right), \qquad (1)$$

where the isoscalar densities are the total $(n+p)$ densities, while the isovector densities are the differences of the neutron and proton $(n-p)$ densities. The energy densities $\mathcal{H}_t^{even}(\boldsymbol{r})$ and $\mathcal{H}_t^{odd}(\boldsymbol{r})$ are the real, time-even, scalar, and isoscalar functions of local densities and their derivatives. The time-even part of Skyrme EDF

$$\begin{aligned} \mathcal{H}_t^{even}(\boldsymbol{r}) = {} & C_t^{\rho}[\rho_0]\rho_t^2 + C_t^{\Delta\rho}\rho_t\Delta\rho_t + C_t^{\tau}\rho_t\tau_t \\ & + C_t^{J0}\mathcal{J}_t^2 + C_t^{J1}\boldsymbol{J}_t^2 + C_t^{J2}\mathfrak{J}_t^2 \\ & + C_t^{\nabla J}\rho_t\boldsymbol{\nabla}\cdot\boldsymbol{J}_t, \end{aligned} \qquad (2)$$

is expressed as a bilinear form of the time-even densities and their derivatives. The time-odd Skyrme EDF

$$\begin{aligned} \mathcal{H}_t^{odd}(\boldsymbol{r}) = {} & C_t^{s}[\rho_0]\boldsymbol{s}_t^2 + C_t^{\Delta s}\boldsymbol{s}_t\cdot\Delta\boldsymbol{s}_t + C_t^{T}\boldsymbol{s}_t\cdot\boldsymbol{T}_t + C_t^{j}\boldsymbol{j}_t^2 \\ & + C_t^{\nabla j}\boldsymbol{s}_t\cdot(\boldsymbol{\nabla}\times\boldsymbol{j}_t) \\ & + C_t^{\nabla s}(\boldsymbol{\nabla}\cdot\boldsymbol{s}_t)^2 + C_t^{F}\boldsymbol{s}_t\cdot\boldsymbol{F}_t, \end{aligned} \qquad (3)$$

contains all time-odd densities and their derivatives written in a bilinear form. The terms proportional to the coupling constants $C_t^{\nabla s}$ and C_t^{F} occur for tensor force only and both are equal zero in the standard parametrizations of the Skyrme effective interactions.

Invariance under local gauge transformations of the Skyrme energy density (1) links pairs of time-even and time-odd terms in the energy functional provided that the coupling constants fulfill the constraints [32]:

$$\begin{aligned} C_t^{\tau} &= -C_t^{j}, \\ C_t^{J0} &= -\tfrac{1}{3}C_t^{T} - \tfrac{2}{3}C_t^{F}, \\ C_t^{J1} &= -\tfrac{1}{2}C_t^{T} + \tfrac{1}{4}C_t^{F}, \\ C_t^{J2} &= -C_t^{T} - \tfrac{1}{2}C_t^{F}, \\ C_t^{\nabla J} &= C_t^{\nabla j}. \end{aligned} \qquad (4)$$

The spin-orbit terms are proportional only to $C_t^{\nabla J}{=}C_t^{\nabla j}$ in the standard Skyrme functionals. However, with the generalized spin-orbit interaction (with the full isovector freedom in the spin-orbit term [33])

$$\begin{aligned} C_0^{\nabla J} &= -b - \tfrac{1}{2}b', \\ C_1^{\nabla J} &= -\tfrac{1}{2}b', \end{aligned} \tag{5}$$

where b and b' are the new parameters.

Four zero-order coupling constants of the Skyrme EDF ($C_t^{\rho}[\rho_0]$, $C_t^{s}[\rho_0]$) can be expressed in terms of the Skyrme force parameters [34] (t_0, x_0, t_3, x_3, α) and the rest (24 second-order) coupling constants can be expressed in terms of the other seven Skyrme force parameters (t_1, x_1, t_2, x_2, W_0, t_e, t_o), and therefore, the time-odd coupling constants in the Skyrme EDF are linear combination of the time-even ones [32], see also Ref. [26, 28, 29] for further discussion.

The total energy in the Skyrme-HFB approach is

$$\begin{aligned} E^{tot}[\bar{\boldsymbol{\rho}}] &\equiv E^{tot}\left[\rho, \tau, \mathbb{J}; \boldsymbol{s}, \boldsymbol{T}, \boldsymbol{j}, \boldsymbol{F}; \tilde{\rho}\right] \\ &= \int \mathrm{d}^3\boldsymbol{r}\left(\mathcal{E}_{kin}(\boldsymbol{r}) + \mathcal{E}_{Sk}(\boldsymbol{r})\right) \\ &\quad + \int \mathrm{d}^3\boldsymbol{r}\left(\mathcal{E}^{dir}_{Coul}(\boldsymbol{r}) + \mathcal{E}^{ex}_{Coul}(\boldsymbol{r})\right) \\ &\quad + \int \mathrm{d}^3\boldsymbol{r}\mathcal{E}_{pair}(\boldsymbol{r}) + E_{corr}, \end{aligned} \tag{6}$$

where $\mathcal{E}_{kin} = \tau_0(\boldsymbol{r})(\hbar^2/2m)$ is a kinetic energy density of both protons and neutrons (for the neutron and proton masses being approximated by their average value), $\mathcal{E}_{Sk}$ is the Skyrme EDF, Eq. (1), and $\mathcal{E}^{dir}_{Coul}$, $\mathcal{E}^{ex}_{Coul}$ is a direct and an exchange Coulomb energy density, respectively.

The $\mathcal{E}_{pair}$ is the isovector $|T_z|$ =1 pairing energy density, corresponding to a density-dependent delta interaction

$$\mathcal{E}_{pair} = \sum_{q=p,n} \frac{V_q^0}{4}\left[1 - V^1\left(\frac{\rho_0(\boldsymbol{r})}{\rho_{st}}\right)^{\beta}\right]\tilde{\rho}_q^2(\boldsymbol{r}), \tag{7}$$

where ρ_{st} is the saturation density of nuclear matter that approaches the density inside the nucleus, $\beta = 1$ (usually), and $V^1 = 0$, 1, or 1/2 for *volume*-, *surface*-, or *mix*-type pairing, and $\tilde{\rho}_q(\boldsymbol{r})$ is the paring density for protons and neutrons [35]. The volume pairing interaction acts primarily inside the nuclear volume, while the surface pairing acts on the nuclear surface. A correction term, E_{corr}, includes corrections for spurious motions caused by symmetry violation in the mean-field approximation [36].

B. The method of Lagrange multipliers

The constrained and/or cranked Skyrme-HF(B) approach is equivalent to minimization of the E^{tot} EDF, Eq. (6), with respect to the densities and currents. Using the method of Lagrange multipliers we solve an equality-constrained problem (ECP) for the objective function E^{tot}:

$$\begin{cases} \min\limits_{\bar{\boldsymbol{\rho}}} E^{tot}[\bar{\boldsymbol{\rho}}] \\ \text{subject to: } \langle \hat{N}_q \rangle = N_q, \quad (q = p, n), \\ \qquad\qquad\quad \langle \hat{Q}_{\lambda\mu} \rangle = Q_{\lambda\mu}, \\ \qquad\qquad\quad \langle \hat{J}_i \rangle = I_i, \quad (i = x, y, z), \end{cases} \tag{8}$$

where the constraints are defined by average values $N_{p/n} = Z$ or N for the proton and neutron particle-number operator $\hat{N}_{p/n}$, the constrained values $Q_{\lambda\mu}$ for the mass-multiple-moment operators $\hat{Q}_{\lambda\mu}$, and the constrained value I_i for the angular momentum operator $\hat{J}_i$ along the i-axes.

To solve the above ECP one can use the standard method of Lagrange multipliers, *e.g.*, the quadratic penalty method, or the augmented Lagrangian method. A comparison of both methods can be found in Ref. [37].

The augmented Lagrangian functional (or Routhian) associated with ECP is defined as

$$\begin{aligned} E_c'[\bar{\boldsymbol{\rho}}, \boldsymbol{\lambda}, \boldsymbol{\Lambda}, \boldsymbol{\omega}] = E^{tot}[\bar{\boldsymbol{\rho}}] &- \sum_{q=p,n} \lambda_q \langle \hat{N}_q \rangle \\ &+ \sum_{\lambda\mu} C_{\lambda\mu}\Big(\langle \hat{Q}_{\lambda\mu} \rangle - Q_{\lambda\mu}\Big)^2 \\ &+ \sum_{\lambda\mu} \Lambda_{\lambda\mu}\Big(\langle \hat{Q}_{\lambda\mu} \rangle - Q_{\lambda\mu}\Big) \\ &- \sum_{i=x,y,z} \omega_i \langle \hat{J}_i \rangle \end{aligned} \tag{9}$$

where λ_p, λ_n, $\Lambda_{\lambda\mu}$, and ω_i are the *Lagrange multipliers*, and $C_{\lambda\mu}$ >0 are the *penalty parameters*. In the ALM the Lagrange multipliers $\Lambda_{\lambda\mu}$ are iterated according to

$$\Lambda^{k+1}_{\lambda\mu} = \Lambda^{k}_{\lambda\mu} + 2C^{k}_{\lambda\mu}\Big(\langle \hat{Q}_{\lambda\mu} \rangle - Q_{\lambda\mu}\Big), \tag{10}$$

see, Ref. [37] and references cited therein.

In an adiabatic approximation nuclear collective and intrinsic degrees of freedom can be decoupled and the collective motion of nucleus can be described in terms of a few collective variables describing shape evolution. Using a primal function of ECP

$$E^{tot}(Q_{\lambda\mu}; \boldsymbol{I}) = \min_{\langle \hat{Q}_{\lambda\mu} \rangle = Q_{\lambda\mu},\, \langle \hat{J}_i \rangle = I_i} E^{tot}[\bar{\boldsymbol{\rho}}], \tag{11}$$

one can characterize these shapes by the mean values of external fields represented by the multipole-moments and angular momentum operators.

C. The Skyrme-HFB calculations

The Hartree-Fock wave function is the Slater determinant of single particle orbitals. Thus the orbitals depend on the single particle Hamiltonian $\hat{h}$, which depends on the densities and currents. The densities and currents in turn depend on the orbitals, so we must solve ECP, Eq. (8), self-consistently (by iteration until convergence).

The above ECP was solved using the augmented Lagrangian method with the symmetry-unrestricted code HFODD [38] which solves the Skyrme-HFB equations in the Cartesian deformed harmonic-oscillator (h.o.) basis. In the particle-hole channel the Skyrme SkM* force [39] was applied and a density-dependent *mixed* pairing [1, 40] interaction with the parameters $V_n^0 = -268.9$ MeV fm^3 and $V_p^0 = -332.5$ MeV fm^3 in the particle-particle channel was used.

The code HFODD calculates parameters of the h.o. basis using geometrical consideration [41]. The relative values of the frequencies of the deformed h.o. in the three Cartesian directions are defined by the condition $\omega_x R_x = \omega_y R_y = \omega_z R_z$, while the overall factor is given by $(\omega_x\omega_y\omega_z)^{1/3} = \omega_0$, where $\hbar\omega_0 = f \times 41$ MeV$/A^{1/3}$ is the spherical h.o. frequency and f=1.2 is a scaling factor [41]. In the above condition, R_x=$R(\pi/2, 0)$, R_y=$R(\pi/2, \pi/2)$, and R_z=$R(0, 0)$ are the lengths of principal axes of a sharp-edge reference body surface, defined by deformation parameters $\alpha_{\lambda\mu}$ in terms of multipole expansion

$$R(\theta,\phi) = c(\alpha)\Big(1 + \sum_{\lambda=0}^{\lambda_{max}} \sum_{\mu=-\lambda}^{\lambda} \alpha_{\lambda\mu} Y_{\lambda\mu}(\theta,\phi)\Big), \qquad (12)$$

where $c(\alpha)$ is a function of $\alpha_{\lambda\mu}$ such that the volume enclosed by the surface does not depend on α. In the present study, we have used the axially deformed h.o. basis with the deformation parameter α_{20} chosen to be equal to the mean-field value calculated in the code for a given value of $\langle\hat{Q}_{20}\rangle$, *cf.* Eq. (1.35) of Ref. [12] and Ref. [42]. For example, this procedure for the quadrupole moment constraint $Q_{20} = -200$ b gives $\alpha_{20} = -0.70$ which corresponds to $\hbar\omega_\perp$=$\hbar\omega_x$=$\hbar\omega_y$ = 5.96 MeV and $\hbar\omega_z$ = 11.03 MeV. We keep this deformed h.o. basis when we examine toroidal shapes with the large oblate deformation $Q_{20} < -200$ b. The basis was composed of the 1140 lowest states taken from the N_0=26 h.o. shells. With this basis size, our tests show that we can properly describe toroidal shapes up to $Q_{20} \gtrsim -600$ b deformation.

Our objective is to locate local toroidal figures of equilibrium, if any, in the multi-dimensional search space of $\{A, Q_{20}, I\}$. We first use the quadrupole moment Q_{20} constrained Skyrme-HFB approach to search for the nuclear density distributions with toroidal shapes. Next, using as starting configurations the toroidal solutions we apply the constrained and cranked around the symmetry z-axis Skyrme-HF approach to map out the energy landscape for axially-symmetric toroidal shapes under Q_{20} and I=I_z constraints. If the states with I=I_z as a function of Q_{20} deformation reveal a local energy minimum then the quadrupole constraint is removed at that minimum and symmetry-unrestricted free-convergence is tested to ensure that the non-collectively rotating toroid nucleus is indeed a figure of equilibrium. It is worth noting that in the unconstrained and symmetry-unrestricted cranked Skyrme-HF calculations we do not impose the axial and reflection symmetries to the toroidal system to ensure its stability with respect to these modes.

D. Pairing correlations

As mentioned above, in the present calculations we use the constrained Skyrme-HFB approach only during the first stage of our method, when we try to establish the region of Q_{20} deformation with the toroidal solutions. In the following calculations we apply the cranked Skyrme-HF model (neglecting the pairing correlations) trying to locate the THSIs.

A quantal system such as axially symmetric toroid cannot rotate around a symmetry axis. In the cranking approach the Lagrangian multiplier ω_z allows one to solve the ECP (8) with a supplementary condition on an angular momentum $\langle\hat{J}_z\rangle = I_z$, where the z-axis is choose as the symmetry axis. The total angular momentum I=I_z, in a case when ω_x= ω_y=0, is built up by selecting nucleonic orbitals that are most favorable in creating the states with required angular momentum and with the lowest energy, the so-called optimal configurations (*cf.* Refs. [10–15]). This non-collective rotation around the symmetry axis is permissible quantum mechanically only by particle-hole excitations with respect to the uncranked state, leading to aligned single-particle angular momenta along the symmetry axis

$$\begin{aligned} I_z = \langle\hat{J}_z\rangle &= \sum_{i=1}^{A}\langle\hat{j}_z\rangle_i = \sum_{i}^{A}(\Omega_z)_i \\ &= \sum_{i\ exc}\left(\Omega_z^{part} - \Omega_z^{hole}\right)_i, \end{aligned} \qquad (13)$$

where $\Omega_z = \Lambda_z \pm 1/2$ denotes the projection of the single-particle angular momentum onto the symmetry z-axis and in the second equation the sum runs over the particle-hole excitations.

The Cooper pairs in a nucleus are composed of the pairs of nucleons in the time-reversal conjugate orbitals with $\Omega_z = \pm\Omega$. The pairing correlation diminishes with each particle-hole excitation which successively breaks down the Cooper pairs. When the seniority of a configuration increases, the blocking effect [12, 15] is effective in reducing the pairing correlations in the toroidal high-spin states. We neglect the pairing in the present study of the THSIs. It would certainly be interesting to examine the effect of weak pairing correlations on toroidal high-spin isomers, but that will be left for a future study.

III. RESULTS AND DISCUSSIONS

A. Toroidal system of $^{304}120_{184}$ without spin

Using the above self-consistent Skyrme-HFB mean-field theory, we study first the nucleus $^{304}120_{184}$ under the constraint of a fixed Q_{20} without spin. We obtain the total energy of the system with a toroidal density as a function of the constrained Q_{20}, as shown in Fig. 2. It indicates that even though $^{304}120_{184}$ without spin may have a toroidal density for $Q_{20} \leq$ -158 b, its total energy curve as a function of Q_{20} lies on a slope. This implies that the toroidal system of $^{304}120_{184}$ without spin is unstable against the tendency to return to a sphere-like geometry, *cf.* Ref. [25]. For future exploration of possible superheavy toroidal nuclear system without spin, it will be necessary to go to systems with a greater charge numbers with $Z \geq 122$ as in Ref. [7] or alternatively to find single-particle "shells" in proton and neutron numbers in regions of sparse single-particle level densities at the top of the Fermi surface, for which the shell effects may provide a sufficiently shell correction [43] to stabilize a toroidal nuclear system.

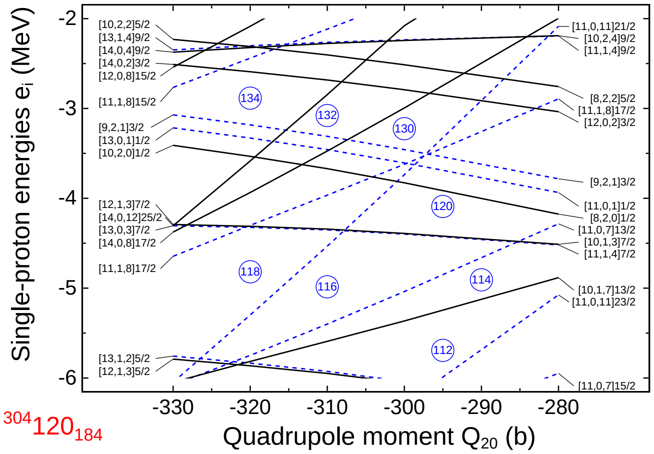

FIG. 3. (Color online) Proton single-particle levels in the canonical basis for $^{304}120_{184}$ in the toroidal configuration as a function of the constraining quadrupole moment Q_{20}, obtained in the Skyrme-HFB calculations. The levels with positive parity are drawn with solid (black) lines, while those with negative parity are drawn with gray dashed (blue color) lines. The circled numbers denote the occupation numbers at regions of spare single-particle energy level density ("shells").

To study the shell effects in superheavy toroidal nuclear system without spin, we examine the single-particle states of $^{304}120_{184}$ with a toroidal density as a function of the quadrupole moment Q_{20} in self-consistent Skyrme-HFB calculations. The self-consistent single-particle potential will also assume a toroidal shape. The proton and neutron single-particle energy levels (in the canonical basis) for $^{304}120_{184}$ are shown in Fig. 3 and in Fig. 4, respectively. Each single-particle state is labeled by the Nilsson quantum numbers $[N, n_z, \Lambda]\Omega$ of the dominant component, and is twofold degenerate, with $\Omega_z = \pm\Omega$. Solid and dashed curves are used to distinguish positive and negative parity levels, respectively. We find from Figs. 3 and 4 that the densities of neutron and proton single-particle states are far from uniform. There are regions of sparse single-particle level densities which can be identified as the "shells" associated with enhanced stability [43]. For brevity of notation, we shall call these shells associated with a toridal nuclear density and potential the *toroidal* shells.

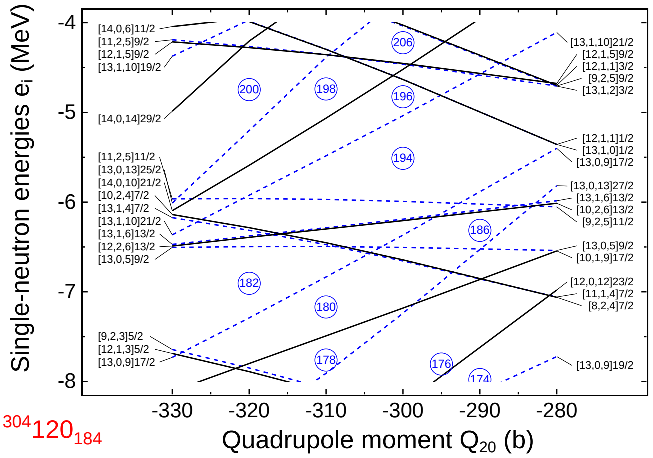

FIG. 4. (Color online) The same as in Fig. 3, but for the neutron single-particle levels.

For the nucleus $^{304}120_{184}$ in the toroidal configuration at $Q_{20} \approx -300$ b, Figs. 3 and 4 show that the proton Fermi surface for $Z = 120$ resides in the low single-particle level density region of a proton shell at $Z = 120$, but the neutron Fermi surface for $N = 184$ resides in a region of high single-particle level density. The stabilizing effects for the *toroidal* proton shell at $Z = 120$ with a negative proton shell correction is counter-balanced by the destabilizing effect for $N = 184$ with a positive neutron shell correction, in the region of deformation $Q_{20} \approx -300$ b. Furthermore, the bulk Coulomb interaction in $^{304}120_{184}$ nucleus is just below the threshold to open up a hole for a toroidal system, as it is for a nucleus with $Z \geq 122$ [7]. As a consequence, in the Skyrme-HFB approach which takes into account both the bulk properties and the shell effects, the combined total energy of $^{304}120_{184}$ without spin in the toroidal configuration does not possess an energy minimum as a function of Q_{20}.

Even though Figs. 3 and 4 pertain to the self-consistent single-particle states for $^{304}120_{184}$, we expect that as the mean-field potential varies only slightly as a function of the atomic number and the neutrons number, and it depends more sensitively on the spatial shape of the nuclear density distribution, the single-particle state diagrams in Figs. 3 and 4 can therefore be approximately applied as single-particle states for the deformations Q_{20} in the toroidal configuration in an extended region around

$^{304}120_{184}$. One can therefore read out various *toroidal* shells for protons and neutrons at various deformations Q_{20} in Figs. 3 and 4. One finds proton shells at Z=116, 118, 120, 132, 134, and neutron shells at N=180, 182, 186, 194, and 198. In our future work, we will exploit the property of the extra stability of superheavy nuclei for which the *toroidal* proton and neutron shells are located at the same deformation.

B. Construction of toroidal configurations of $^{304}120_{184}$ with high spin

As the toroidal configurations of $^{304}120_{184}$ nucleus are unstable without spin, we like to examine here whether toroidal $^{304}120_{184}$ may be stabilized when it possesses an angular momentum aligned along the symmetry axis such that I=I_z. Following Bohr and Mottelson [11], we can construct a nucleus with an aligned angular momentum I_z by particle-hole excitations. Specifically, referring to the single-particle states in Figs. 3 and 4 for toroidal system of $^{304}120_{184}$ at $Q_{20} = -300$ b without spin, we can make a hole at a state with angular momentum component $-|\Omega_z^{hole}|$ and place it at a particle state with angular momentum Ω_z^{part}. The particle-hole pair will generate an aligned angular momentum I_z of magnitude $\Omega_z^{part} + |\Omega_z^{hole}|$, see, Eq. (13). By making many such particle-hole excitations, a nucleus with a very high spin, I=I_z, can be constructed, especially when the number of particle-hole excitations and the magnitudes $|\Omega_z|$ of these participating particle and hole states are large. Because I_z depends on Ω_z and the number of particle-hole excitations, it assumes quantized non-trivial values that can only be obtained from a detailed examination of the structure of the single-particle state energy diagram of the nucleus of interest.

There are two equivalent ways to construct a high-spin state with the spin aligned along the symmetry axis: (i) the method of employing the tilted Fermi surfaces, and (ii) the plots of the single-particle Routhians $e_i' = e_i - \hbar\omega(\Omega_z)_i$ as a function of $\hbar\omega$.

The single-particle energy level diagram at a fixed quadrupole moment, say $Q_2 = -300$ b, can be expanded out to include the additional dependence of Ω_z as the horizontal axis, as shown in Figs. 5 and 6. The Fermi surface for this case without spin shows up as a horizontal line and all levels below it are occupied, see, an inset in Fig. 5. A high-spin state can be constructed by tilting the Fermi level in the expanded single-particle diagram, *cf.* Ref. [13]. The degree of tilt can be specified in the Skyrme-HF calculations by the Lagrange multiplier $\hbar\omega$ which describes the constraint I_z=$\langle\hat{J}_z\rangle$= $\sum_{i=1}^{A}(\Omega_z)_i$, with each I=I_z spanning a small region of $\hbar\omega$ [12].

We collect in Table I the particle-hole excitation configurations leading to the states of $^{304}120_{184}$ with $I_z = 81$ and 208. They are particle-hole excitations relative to the Skyrme-HFB states without spin, as labeled by the quantum numbers $[N, n_z, \Lambda_z]\Omega_z$ for the optimal toroidal configurations of $^{304}120_{184}$ at $Q_{20} = -300$ b in Figs. 5 and 6.

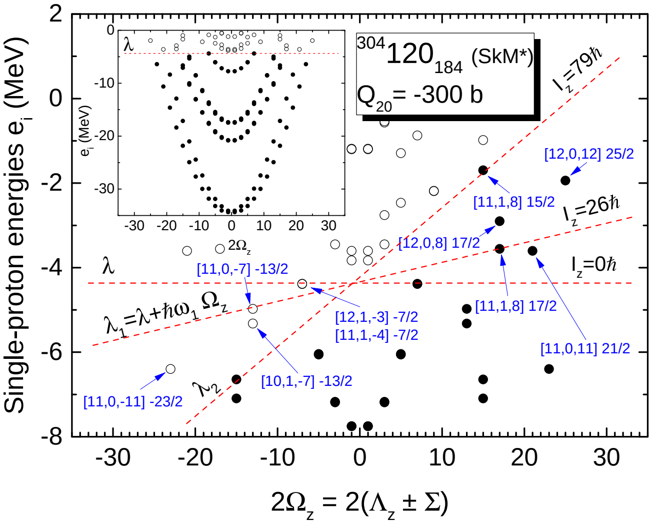

FIG. 5. (Color online) The proton single-particle energy levels of $^{304}120_{184}$ in the toroidal configuration at $Q_{20} = -300$ b, as a function of $2\Omega_z$. The thin gray dashed (red color) lines give the tilted proton Fermi surfaces which lead to the proton spin value I_z=26 for $\hbar\omega_1$≈0.1 MeV, and I_z=79 at $\hbar\omega_2$≈0.28 MeV. In the case of I_z=79, the occupied states are shown as solid circular points, and the unoccupied states as open circles.

TABLE I. The particle-hole excitation configurations leading to the states of $^{304}120_{184}$ with I_z=I_z(proton) +I_z(neutron)=26+55=81 and I_z=79+129=208.

	Hole states	Particle states
I_z(proton)=26	[11,1,-4] -7/2	[11,0,11] 21/2
	[12,1,-3] -7/2	[11,1,8] 17/2
I_z(proton)=79	[11,0,-7] -13/2	[12,0,8] 17/2
	[10,1,-7] -13/2	[12,0,12] 25/2
	[11,0,-11] -23/2	[11,1,8] 15/2
I_z(neutron)=55	[10,2,-4] -7/2	[13,0,5] 9/2
	[11,1,-4] -7/2	[13,0,9] 17/2
	[10,1,-9] -17/2	[13,1,6] 13/2
	[13,0,-13] -27/2	[10,2,6] 13/2
I_z(neutron)=129	[12,0,-12] -23/2	[9,2,5] 11/2
	[13,0,-9] -19/2	[13,1,10] 21/2
	[12,1,-9] -19/2	[14,0,10] 21/2
	[10,2,-4] -9/2	[13,0,13] 25/2

In addition to the tilted Fermi surface method, there is another equivalent method using the diagrams of single-particle Routhians vs. $\hbar\omega$. Upon using a Lagrange multiplier $\hbar\omega$ to describe the constraint of an aligned angular momentum I=I_z along the symmetry z-axis, the constrained single-particle Hamiltonian becomes $\hat{h}' = \hat{h} - \hbar\omega\hat{j}_z$, where $\hat{j}_z$ is the z-component of the single-particle angular momentum operator along the symmetry axis with eigenvalue Ω_z. The single-particle Routhian

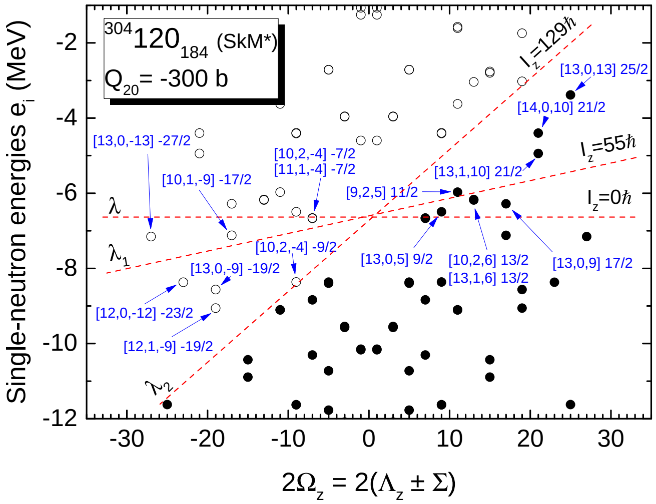

FIG. 6. (Color online) The neutron single-particle energy levels of $^{304}120_{184}$ in the toridal configuration at $Q_{20} = -300$ b, as a function of $2\Omega_z$. The thin dashed lines give the tilted neutron Fermi surfaces which lead to the neutron spin value I_z=55 for $\hbar\omega_1$≈0.1 MeV, and I_z=129 for $\hbar\omega_2$≈0.28 MeV. In the case of I_z=129, the occupied states are shown as solid circular points, and the unoccupied states as open circles.

e'_i is the eigenvalues of $\hat{h}'$ for the single-particle state i. A nucleus in the state with a total aligned angular momentum I_z along the symmetry axis can be constructed by populating states below the Fermi level in the single-particle Routhian level diagram. As the Routhian $e'_i(\hbar\omega)$ for the state Ω_z is shifted from the corresponding single-particle energy without spin $e'_i|_{\hbar\omega=0}$ by a term proportional to $-\hbar\omega(\Omega_z)_i$, different Lagrange multipliers $\hbar\omega$ will result in different ordering of the single-particle Routhians and different I_z, for a given occupation number Z or N. In Figs. 7 and 8, we give the proton and neutron single-particle Routhians as a function of the constraining Lagrange multiplier $\hbar\omega$, for a toroidal system of $^{304}120_{184}$ with $Q_{20} = -300$ b, obtained in self-consistent cranked Skyrme-HF calculations.

We can use single-particle Routhians in Figs. 7 and 8 to determine I_z as a function of the nucleon occupation number $N_{p/n}$ and $\hbar\omega$. For a given $N_{p/n}$ and $\hbar\omega$, the aligned I_z angular momentum can be obtained by summing Ω_z over all states below the Fermi surface, *cf.* Eq. (13). For the occupation numbers of $Z = 120$ and $N = 184$ in Figs. 7 and 8, there are shells, regions of low Routhian energy level density, for different I_z configurations at different values of $\hbar\omega$. They represent configurations with relative enhanced stability [5, 43]. In the corresponding Skyrme-HF calculation, they may lead to local energy minima for various allowed angular momenta.

Figure 7 shows that for the proton occupation number $Z = 120$, possible shells are located at I_z(proton)=0, 26, 41, 60, and 79 at different values of $\hbar\omega$. Figure 8 shows that for the neutron occupation number $N = 184$, possible shells are I_z(neutron)=0, 20, 55, 92, 112, and 129 at various values of $\hbar\omega$. For a nucleus to have a local minimum with a total aligned angular momentum I_z=I_z(proton)+I_z(neutron), the $\hbar\omega$ locations of the proton and neutron shells, need to be close to each other. We find that by combining the proton and neutron spins, the total spin of the system can be I_z= 81 at $\hbar\omega$≈0.1 MeV, and I_z=208 at $\hbar\omega$≈0.28 MeV, for $Q_{20} = -300$ b.

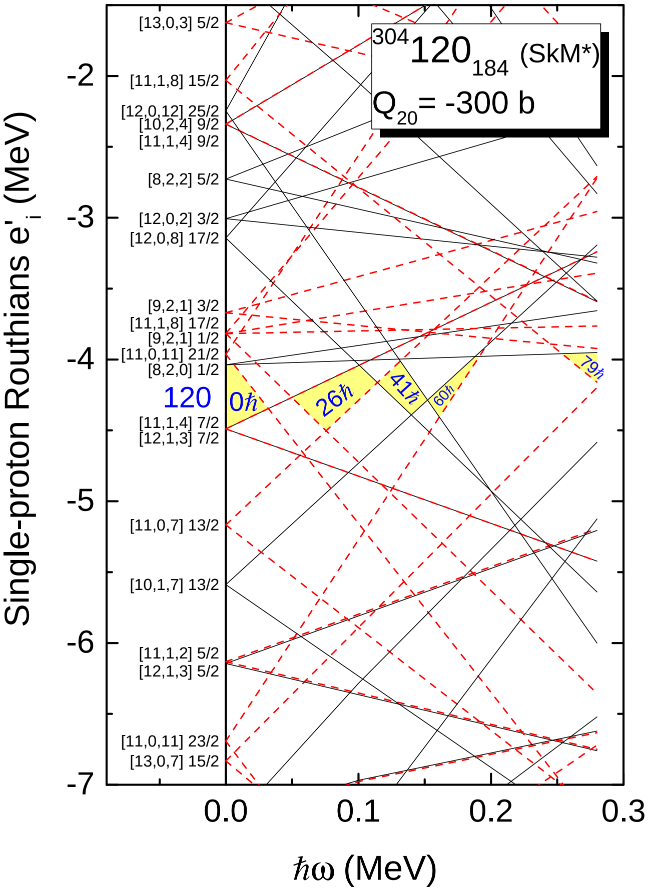

FIG. 7. (Color online) Proton single-particle Routhians of $^{304}120_{184}$ in the toroidal configuration with Q_{20}=−300 b, as a function of the cranking frequency $\hbar\omega$. The states are labeled by the Nilsson quantum numbers $[N, n_z, \Lambda]\Omega$. Solid (black) and dark gray dashed (red color) curves are used to distinguish even and odd principal quantum number states, respectively. The aligned angular momenta I_z for $Z = 120$ protons are shown at various $\hbar\omega$ locations.

Referring to the proton single-particle Routhians diagram at $\hbar\omega$≈0.1 MeV in Fig. 7, the proton spin of I_z(proton)=26 for the 2p-2h excitation arises by emptying the [11,1,-4]-7/2 and [12,1,-3]-7/2 states, and occupying [11,0,11]21/2 and [11,1,8]17/2 states. This result in the alignment of I_z=7 from the holes, I_z=19 from particles, and I_z(proton)=7+19=26, *cf.* Eq. (13). In Fig. 8, the neutron spin of I_z(neutron)=55 arises by emptying [10,2,-4]-7/2, [11,1,-4]-7/2, [10,1,-9]-17/2, and [13,0,-13]-27/2 states, and populating [13,0,5]9/2, [13,0,9]17/2, [13,1,6]13/2, and [10,2,6]13/2 states. This results in I_z(neutron)= 29+26=55 for which the neutron holes provide 29 units, and the neutron particles 26. The total spin of the toroidal system of $^{304}120_{184}$ at $\hbar\omega\approx$0.1 MeV is I_z=I_z(proton)+I_z(neutron)=26+55=81.

For the nuclear total spin of I_z=208 at $\hbar\omega\approx$0.28 MeV, one observes from Fig. 7 that the proton spin of I_z(proton)=79 from the 5p-5h excitation arises by emptying the proton states [11,1,-4]-7/2, [12,1,-3]-7/2, [11,0,-7]-13/2, [10,1,-7]-13/2, and [11,0,-11]-23/2, and occupying proton states [11,0,11]21/2, [11,1,8]17/2, [12,0,8]17/2, [12,0,12]25/2, and [11,1,8]15/2. This result in the alignment of I_Z=(63/2) from the holes, and I_Z=(95/2) from particles. The proton 5p-5h excitation gives I_z(proton)=(63/2)+(95/2)=79. In Fig. 8, the neutron spin of I_z(neutron)=129 arises from the 8p-8h excitation by emptying [10,2,-4]-7/2, [11,1,-4]-7/2, [10,1,-9]-17/2, [13,0,-13]-27/2, [12,0,-12]-23/2, [13,0,-9]-19/2, [12,1,-9]-19/2, [10,2,-4]-9/2 states, and populating [13,0,5]9/2, [13 ,0 ,9]17/2, [13,1,6]13/2, [10,2,6]13/2, [9,2,5]11/2, [13,1,10]21/2, [14,0,10]21/2, and [13,0,13]25/2 states. The neutron 8p-8h excitation gives I_z(neutron)=64+65=129.

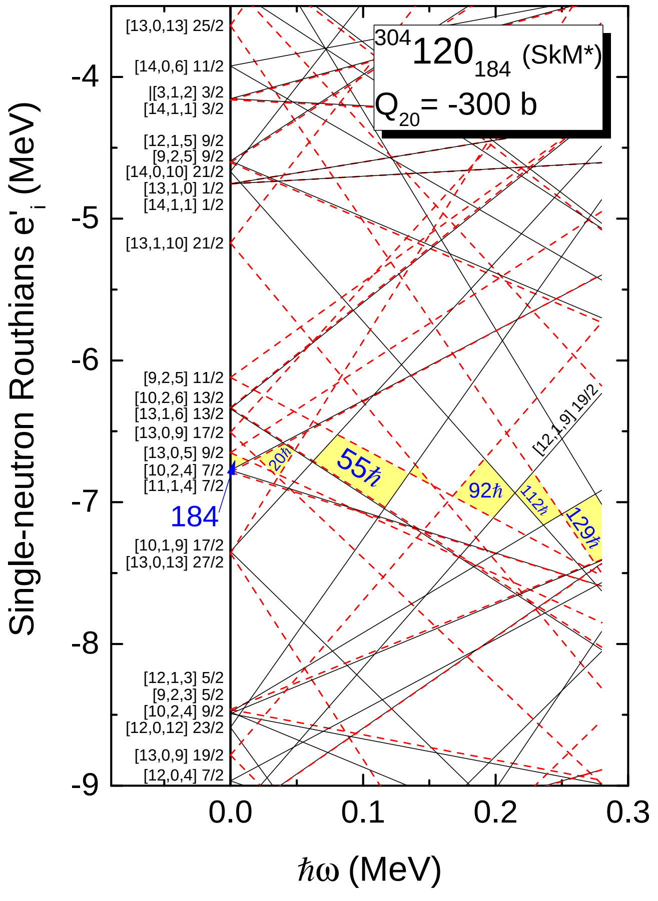

FIG. 8. (Color online) The same as in Fig. 7, but for the neutron single-particle Routhians of $^{304}120_{184}$ in the toroidal configuration. The aligned angular momenta I_z for $N = 184$ neutrons are shown at various $\hbar\omega$ locations.

The self-consistent single-particle Hamiltonian $\hat{h}'$ under an aligned angular momentum constraint depends on the Hamiltonian operator $\hat{h}$ that is a self-consistent function of the nuclear density and nuclear current. The latter nuclear current depends on the aligned angular momenta I_z, which depends in turn on the Lagrange multiplier $\hbar\omega$. Therefore, the single-particle Routhian, e_i', which is the eigenvalue of $\hat{h}'$, can acquire an additional self-consistency dependence on $\hbar\omega$, in addition to the explicit dependency on $-\hbar\omega\Omega_z$. We find that the self-consistent Skyrme-HF single-particle Routhians $e'_{Nn_z\Lambda_z\Omega_z}(\hbar\omega)$ in Figs. 7 and 8 can be approximately represented by

$$e'_{Nn_z\Lambda_z\Omega_z}(\hbar\omega) \approx e'_{Nn_z\Lambda_z\Omega_z}|_{\hbar\omega=0} + a\hbar\omega - \hbar\omega\Omega_z, \qquad (14)$$

where the additional term $a\hbar\omega$ with a parameter $a \approx 0.5$ arises from the *effect of self-consistency* of the single-particle Routhian Hamiltonian $\hat{h}'$. It affects mostly those states with a small value of Ω_z and is un-important for states with large Ω_z. In the present case for proton occupation number at $Z = 120$, an Ω_z =1/2 state occurs by chance at the top to the Fermi surface, as in Fig. 7.

C. The toroidal high-spin isomers in $^{304}120_{184}$

The tilted Fermi surface method or the Routhian single-particle method in the last subsection deals only with the construction of a state with an aligned angular momentum along the toroidal symmetry axis. The question of the stability for such a nucleus needs to be examined by studying the dependence of the total energy as a function of Q_{20} and I_z. The investigation can be carried out by extending the Skyrme-HFB calculations further to include both the quadrupole moment Q_{20} constraint and the angular momentum constraint, I=I_z using a Lagrange multiplier $\hbar\omega$ as the cranking frequency. As stated in Sec. II D we have carried out the cranking calculations without the pairing interaction, using the cranked Skyrme-HF approach.

Applying an additional constraint of an angular momentum $I = I_z$ about the symmetry z-axis in the cranked Skyrme-HF calculations, we search for the energy minima of $^{304}120_{184}$ in the toroidal configuration as a function of the deformation Q_{20} and aligned angular momentum I_z. If a local energy minimum with $I = I_z$ is found, we perform at this point the cranked symmetry-unrestricted and deformation unconstrained Skyrme-HF calculations to locate a stable THSI state in free convergence.

The results of such calculations for $^{304}120_{184}$ are presented in Fig. 9, where we plot the deformation energy (relative to the spherical ground state energy) of the high-spin toroidal states as a function of the constrained Q_{20}, for different quantized I_z. For each point (Q_{20}, I_z) on an I_z curve, it was necessary to adjust $\hbar\omega$ to ensure that the total aligned angular momentum of all nucleons in the occupied states gives the quantized I_z value of interest.

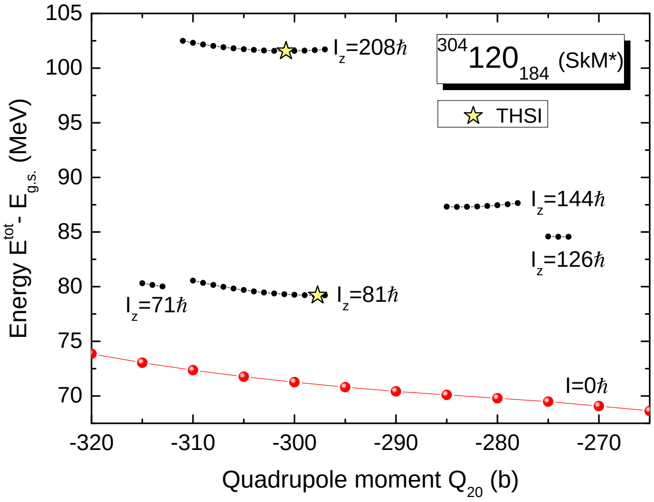

FIG. 9. (Color online) The deformation energies of $^{304}120_{184}$ in the toroidal configuration as a function of the quadrupole moment Q_{20} for I_z=0, 71, 81, 126, 144, and 208. The locations of the toroidal high-spin-isomers (THSIs) for I_z=81 and 208 are indicated by star symbols. All deformation energies are measured relative to the energy of the spherical ground state.

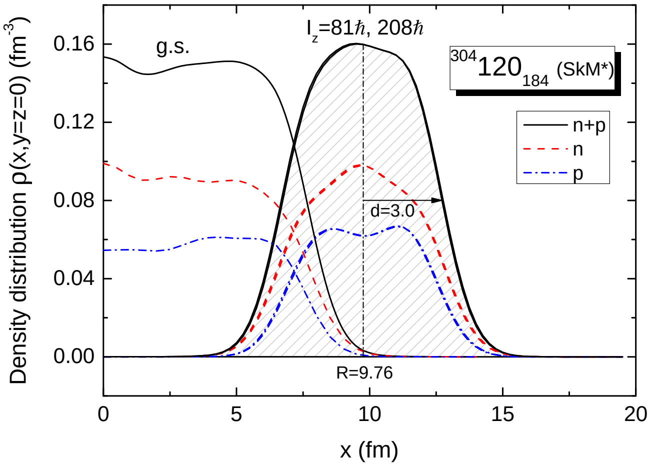

FIG. 10. (Color online) Neuron, proton and total density profiles of the THSIs $^{304}120_{184}$(I=81 and 208) as a function of x for a cut in $y=0$, and $z=0$.

From the energy surface of $^{304}120_{184}$(I_z=81) in the toroidal configuration in Fig. 9, we find that when we vary the constrained Q_{20} with $\hbar\omega\approx$0.1 MeV, the deformation energy of the nucleus in the toroidal configuration as a function of Q_{20} has a minimum. Similarly, from the energy surface of $^{304}120_{184}$(I_z=208), we find that when we vary the constrained Q_{20} with $\hbar\omega\approx$0.28 MeV, the deformation energy of the nucleus as a function of Q_{20} has a minimum. Thus, we have theoretically located two THSI states of $^{304}120_{184}$ with an angular momentum I=I_z=81 (proton 2p-2h, neutron 4p-4h excitation) and I=I_z=208 (proton 5p-5h, neutron 8p-8h) at Q_{20} = −297.7 b and Q_{20} = −300.8 b with energies 79.2 MeV and 101.6 MeV above the spherical ground state energy, respectively. In Fig. 9, deformation energies for I=I_z=126 at $Q_{20}\sim -275$ b and I=I_z=144 at $Q_{20}\sim -280$ b are also exhibited. As there are no energy minima for these I_z states, there are no toroidal high-spin isomers with these aligned angular momenta.

After the THSIs $^{204}120_{184}$ with I=I_z=(81 and 208) have been located, we can examine their properties. Their density profiles as a cut in the plane of positive x is shown in Fig. 10, and as density contours in Fig. 11. The corresponding density profile for the superheavy nucleus in the spherical ground state is also exhibited in Fig. 10. It is interesting to note that the density profiles of the two THSIs with I_z=81 and I_z=208 are nearly the same, as shown indistinguishably in Fig. 10.

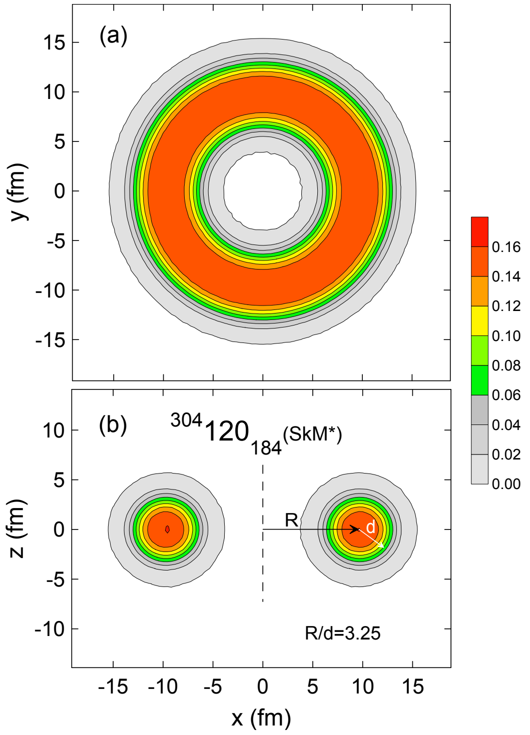

FIG. 11. (Color online) Contours of the total nuclear densities of $^{304}120_{184}$(I_z=81) in cuts: $x-y$ (a), and $x-z$ (b).

One observes in Fig. 10 that the maximum magnitude of the total densities in the $^{204}120_{184}$ THSIs with I=81 and 208 are about the same as those of the nucleus with a spherical shape. This is in contrast to the case of THSI nuclei in the light mass region where the maximum density of the THSI nuclei are only about half of the equilibrium nuclear matter density of the nuclei in the ground state [18]. This arises because the occurrence of THSI nuclei in the light-mass region is dominated by the nuclear shell effect and the occupation of the lowest displaced harmonic oscillator states with n_ρ=n_z=0. For the superheavy nuclei region, the Coulomb repulsion dominates and there are many states involved. Hence, the nuclear density is not greatly affected by the change from a spherical shape to a toroidal shape.

The density contours in Figs. 10 and 11 indicate a well-developed hole in the density of the nucleus. One can characterize the THSI $^{304}120_{184}(I_z = 81)$ by the average geometry parameters of

$$\rho_{\max} = 0.161/\text{fm}^3, \quad R = 9.76 \text{ fm}, \quad d = 3.00 \text{ fm}, \quad (15)$$

which yields $R/d = 3.25$. They have the maximum density close to the nuclear matter density, 0.16 fm^{-3}. The density profile for the THSI at I_z=208 is very similar and will not be exhibited.

IV. SUMMARY

Because of the strong Coulomb repulsion, there is a tendency for the shape of a nucleus with excess charge to bifurcate from a spheroidal into a toroidal shape in the superheavy region. We examine the case of $^{304}120_{184}$. Without spin, the Coulomb repulsion and shell effects are not sufficient to allow an equilibrium toroidal shape for $^{304}120_{184}$. Toroidal minima without spin are possible for superheavy nuclei with greater atomic numbers as reported earlier [7].

The spin of a nucleus with an angular momentum about the toroidal symmetry axis has a stabilizing tendency. We have theoretically located two toroidal high-spin isomeric states of $^{304}120_{184}$ with an angular momentum I=I_z=81 (proton 2p-2h, neutron 4p-4h excitation) and I=I_z=208 (proton 5p-5h, neutron 8p-8h) at $Q_{20} = -297.7$ b and $Q_{20} = -300.8$ b with energies 79.2 MeV and 101.6 MeV above the spherical ground state energy, respectively. The nuclear density distribution of the THSIs $^{304}120_{184}(I_z$=81 and 208) have the maximum density close to the nuclear matter density, 0.16 fm^{-3}, and a toroidal major to minor radius aspect ratio R/d =3.25 with R=9.76 fm.

Our search to locate the THSIs in $^{304}120_{184}$ was focused on the region -320 b $< Q_{20} <$ -265 b of deformation and it is hard to predict whether two found toroidal isomers are yrast states. Figure 9 shows that the $^{304}120_{184}(I_z$=81) THSI may appear to lie on the yrast line as there is no energy minimum with a lower spin lying below this state. Whether the higher $^{304}120_{184}(I_z$=208) THSI state is an yrast state is not known as it depends on the energies of the band of collective states built on the toroidal intrinsic high-spin state of $^{304}120_{184}(I_z$=81), by rotating about an axis perpendicular to the toroidal symmetry axis. A further investigation is required to study this question.

The results of the single-particle state diagrams and Routhian diagrams obtained in the present calculations as a function of deformation Q_{20} and the Lagrange multiplier $\hbar\omega$ indicate that there are shells in the toroidal shape and the spin degrees of freedom. Extra stability can be maintained at appropriate occupation numbers, deformations, and spin. Hence, there may be many toroidal superheavy nuclei as a function of $(Z, N, Q_{20}$, and $I_z)$ that need to be uncovered. The region of toroidal superheavy nuclei may provide an interesting area for further explorations. Future investigations on ways to produce and to detect these states with toroidal densities will be of great interest.

ACKNOWLEDGMENTS

The research was supported in part by the Division of Nuclear Physics, U.S. Department of Energy under Contract DE-AC05-00OR22725 and the National Science Center (NCN), Poland, project No. 2016/21/B/ST2/01227.

---

[1] A. Staszczak, A. Baran, J. Dobaczewski, and W. Nazarewicz, Phys. Rev. C **80**, 014309 (2009).
[2] M. Warda, A. Staszczak and W. Nazarewicz, Phys. Rev. C **86**, 024601 (2012).
[3] A. Staszczak, A. Baran and W. Nazarewicz, Phys. Rev. C **87**, 024320 (2013).
[4] See a reference to J. A. Wheeler's toroidal nucleus in G. Gamow, *Biography of Physics* 1961, (New York: Harper & Brothers Publishers) pp. 297.
[5] C. Y. Wong, Ann. Phys. **77**, 279 (1973).
[6] C. Y. Wong, Phys. Rev. C **17**, 331 (1978).
[7] A. Staszczak and C. Y. Wong, Acta Phys. Pol. B **40**, 753 (2008), and references cited therein.
[8] J. Eggers, Rev. Mod. Phys. **69**, 865 (1997).
[9] E. Pairam and A. Fernández-Nieves, Phys. Rev. Lett. **102**, 234501 (2009).
[10] G. Andersson, S. E. Larsson, G. Leander, P. Möller, S. G. Nilsson, I. Ragnarsson, S. Åberg, R. Bengtsson, J. Dudek, B. Nerlo-Pomorska, K. Pomorski, and Z. Szymański, Nucl. Phys. A **268**, 205 (1976).
[11] A. Bohr and B. R. Mottelson, Nucl. Phys. A **354**, 303c (1981).
[12] P. Ring and P. Schuck, *The Nuclear Many-Body Problem* (Springer-Verlag, Berlin, Heidelberg, New York 1980).
[13] M. J. A. de Voigt, J. Dudek, and Z. Szymański, Rev. Mod. Phys. **55**, 949 (1983).
[14] S. G. Nilsson and I. Ragnarsson, *Shapes and Shells in Nuclear Structure* (Cambridge University Press, New York 1995).
[15] A. V. Afanasjev, D. B. Fossan, G. J. Lane, and I. Ragnarsson, Phys. Rep. **322**, 1 (1999).
[16] T. Ichikawa, J. A. Maruhn, N. Itagaki, K. Matsuyanagi, P-G. Reinhard, and S. Ohkubo, Phys. Rev. Lett. **109**, 232503 (2012).

[17] T. Ichikawa, K. Matsuyanagi, J. A. Maruhn, and N. Itagaki, Phys. Rev. C **89**, 011305(R) (2014).

[18] A. Staszczak and C. Y. Wong, Phys. Lett. B **738**, 401 (2014).

[19] T. Ichikawa, K. Matsuyanagi, J. A. Maruhn, and N. Itagaki, Phys. Rev. C **90**, 034314 (2014).

[20] A. Staszczak and C. Y. Wong, Acta Phys. Pol. B **46**, 675 (2015).

[21] A. Staszczak and C. Y. Wong, Phys. Scripta **90**, 114006 (2015).

[22] A. Staszczak and C. Y. Wong, EPJ Web of Conferences **117**, 0400 (2016).

[23] W. Zhang, H.-Z. Liang, S.-Q. Zhang, and J. Meng, Chin. Phys. Lett. **27**, 102103 (2010) .

[24] A. Baran, M. Kowal, P.-G. Reinhard, L. M. Robledo, A. Staszczak, and M. Warda, Nucl. Phys. A **944**, 442 (2015).

[25] A. Kosior, A. Staszczak, and C. Y. Wong, Acta Phys. Pol. B Proc. Suppl. **10**, 249 (2017).

[26] E. Perlinska, S. G. Rohozinski, J. Dobaczewski, and W. Nazarewicz, Phys. Rev. C **69**, 014316 (2004).

[27] T. Lesinski, M. Bender, K. Bennaceur, T. Duguet, and J. Meyer, Phys. Rev. C **76**, 014312 (2007).

[28] M. Bender, K. Bennaceur, T. Duguet, P.-H. Heenen, T.Lesinski, and J. Meyer, Phys. Rev. C **80**, 064302 (2009).

[29] V. Hellemans, P.-H. Heenen, and M. Bender, Phys. Rev. C **85**, 014326 (2012).

[30] D. Vautherin and D. M. Brink, Phys. Rev. C **5**, 626 (1972); Y.M. Engel, D.M. Brink, K. Goeke, S. Krieger, and D. Vautherin, Nucl. Phys. **A 249**, 215 (1975).

[31] S. G. Rohozinski, J. Dobaczewski, and W. Nazarewicz, Phys. Rev. C **81**, 014313 (2010); Int. J. Mod. Phys. E **19**, 640 (2010).

[32] J. Dobaczewski and J. Dudek, Phys. Rev. C **52**, 1827 (1995); Phys. Rev. C **55**, 3177(E) (1997); Acta Phys. Pol. B **27**, 45 (1996).

[33] P.-G. Reinhard and H. Flocard, Nucl. Phys. **A584**, 467 (1995).

[34] T. H. R. Skyrme, Phil. Mag. **1**, 1043 (1956); Nucl. Phys. **9**, 615 (1959); *ibid.*, p. 635; *ibid.*, p. 641.

[35] J. Dobaczewski, H. Flocard, and J. Treiner, Nucl. Phys. **A422**, 103 (1984).

[36] M. Bender, P.-H. Heenen, and P.-G. Reinhard, Rev. Mod. Phys. **75**, 121 (2003).

[37] A. Staszczak, M. Stoitsov, A. Baran, and W. Nazarewicz, Eur. J. Phys. A **46**, 85 (2010).

[38] N. Schunck, J. Dobaczewski, J. McDonnell, W. Satuła, J. A. Sheikh, A. Staszczak, M. Stoitsov, and P. Toivanen, Comput. Phys. Commun. **183**, 166 (2012).

[39] J. Bartel, P. Quentin, M. Brack, C. Guet, and H. B. Håkansson, Nucl. Phys. **A 386**, 79 (1982).

[40] J. Dobaczewski, W. Nazarewicz, and M. V. Stoitsov, Eur. J. Phys. A **15**, 21 (2002).

[41] J. Dobaczewski and J. Dudek, Comput. Phys. Commun. **102**, 166 (1997); *ibid.* 183 (1997).

[42] J. Dobaczewski, W. Satuła, B. G. Carlsson, J. Engel, P. Olbratowski, P. Pawłowski, M. Sadziak, J. Sarich, N. Schunck, A. Staszczak, M. Stoitsov, M. Zalewski, and H. Zduńczuk, Comput. Phys. Commun. **180**, 2361 (2009).

[43] M. Brack, J. Damgaard, A. S. Jensen, H. C. Pauli, V. M. Strutinsky, and C. Y. Wong, Rev. Mod. Phys. **44**, 320 (1972).